



# Effect of the Quenching and Tempering Temperatures on the Microstructure and Mechanical Properties of H13 Steel

Jian Wang , Zinuo Xu, and Xiaofeng Lu

(Submitted July 25, 2019; in revised form January 21, 2020; published online February 27, 2020)

**H13 steel is a typical hot work die steel with good strength and toughness that is often used to manufacture high-temperature disk springs. However, disk springs occasionally fail after use in the petrochemical industry. Therefore, the effects of the quenching and tempering temperatures on the microstructure and mechanical properties of H13 steel after quenching and tempering processes are investigated herein. The results show that the lath width (lath) controls the strength of the H13 steel. The precipitated phases mainly comprise  $\text{Cr}_{23}\text{C}_6$ ,  $\text{Cr}_7\text{C}_3$  and VC. The coarsening of the  $\text{Cr}_{23}\text{C}_6$  phase reduces the hardness, while reducing the dislocation density improves the toughness of the H13 steels after quenching and tempering. When the quenching temperature is 1040 °C and the tempering temperature is 570 °C, the H13 steel after quenching and tempering has a uniform microstructure with good strength and toughness.**

**Keywords** H13 steel, lath, precipitated phase, quenching temperature, tempering temperature

## 1. Introduction

As a typical air-cooled hardening die steel, H13 steel is widely used in hot forging dies, hot extrusion dies and nonferrous metal die casting dies. The above applications have important requirements for the material properties, such as good toughness, red hardness, thermal fatigue performance and wear resistance (Ref 1-3). In addition, H13 steel is often used to manufacture disk spring products that require good strength and toughness. However, disk spring products made of H13 steel occasionally crack after being applied in the petrochemical industry due to a poor impact toughness and an uneven hardness of the products. Therefore, the performance of H13 steel needs to be optimized to meet the requirements of high-temperature disk springs.

There are two main factors that affect the range of use and service life of H13 steel. First, the isotropy of H13 steel is poor due to banded segregation. Wang et al. (Ref 4) investigated the effects of different temperatures and cooling rates on the banded structure of H13 steel. The results show that the ribbon structure of forgings can be mitigated or even eliminated by high-temperature austenitizing (heating to 1300 °C) with a rapid cooling (oil quenching to room temperature) process. Therefore, the problem of banded segregation can be basically solved.

Second, H13 steel has insufficient thermal strength at high temperatures, especially at 600 °C or higher, and the thermal strength decreases significantly (Ref 5). This is also the key

problem to optimizing the properties of H13 steel for high-temperature disk springs. Relevant scholars have performed many studies and put forward some improvements. Tong et al. (Ref 6) made a “high-silicon and low-molybdenum” adjustment of H13 steel and developed SDH3 steel, which has excellent thermal stability and high-temperature thermal strength. Li et al. (Ref 7, 8) developed a Mo-W series hot working steel with low Si and no Cr. The Mo-W series hot working steel is named SDCM-S steel, and the Mo-W-V series steel is named SDCM-SS steel. The  $\text{M}_2\text{C}$  phase in the Mo-W-V series steel increases the tempering stability, and the  $\text{M}_6\text{C}$  phase in the Mo-W-V series steel has an increased wear resistance due to the delayed precipitation of martensite during the tempering process. All of these properties are optimized by changing the composition of H13 steel.

Without changing the composition, the current comprehensive properties of H13 steel are mainly improved from two aspects, including the purity and the heat treatment process. The improvement in the purity of H13 steel mainly reduces the content of harmful inclusions in the steel through vacuum refining and vacuum consumption. However, these methods are expensive and limited in terms of equipment. In addition, according to statistics, the failure of die casting molds due to improper heat treatment processes is as high as 70% (Ref 9). Therefore, optimizing the heat treatment process is the most economical and effective way to improve the properties of H13 steel. Babu (Ref 10) and others (Ref 11) proposed a double-quenching process. The results show that after a cryogenic treatment and a double-quenching treatment, the carbide particles in the material refine and distribute evenly, and the toughness improves significantly. The thermal stability, high-temperature friction, wear properties and thermal fatigue properties of the steel are also optimized (Ref 12). Yan et al. (Ref 13) and others found that fine grains for H13 steel can be obtained when the quenching temperature is lower than 1080 °C. Excellent mechanical properties can be obtained due to secondary hardening during the tempering process when the tempering temperature is in the range of 550-650 °C. Li

Jian Wang, Zinuo Xu, and Xiaofeng Lu, School of Mechanical and Power Engineering, Nanjing Tech University, Nanjing 211816, China. Contact e-mails: njjwang@njtech.edu.cn and xflu@njtech.edu.cn.

et al. (Ref 14) found that the segregation of primary carbides in H13 steel can be improved after hot forging. As seen from the above results, the heat treatment process is only a means to an end. The structure–property relationship of hot working tool steels is related to the various carbides distributed in the tempered martensite structure (Ref 15). Therefore, it is the ultimate goal to change the internal structure, the grain size, and the type and size of the precipitated phase by an optimized heat treatment process to obtain the properties we need.

In this paper, H13 steel is used as the object to study the relationship between prior austenite grains and mechanical properties under different quenching and tempering temperatures, and the precipitated phases are analyzed in detail. The impact fracture morphologies are studied to analyze the fracture mechanism. The experiments control a single variable, which can study the influence of quenching and tempering accurately. The optimized quenching and tempering temperature range are obtained by microstructure and mechanical property investigations. The above research provides evidence that supports the production of H13 steel for high-temperature disk springs in the future.

## 2. Experimental Materials and Methods

The initial material for the samples used in this experiment comprised an H13 electroslag steel annealed forging (Swedish imported 8407SUPREME), and its chemical composition (wt.%) was measured by mass spectrometry, as shown in Table 1. This conformed to the H13 steel standard specification.

The quenching and tempering heat treatment processes were carried out using a VTO-446 vacuum furnace. The heat treatment process is shown in Fig. 1. The quenching temperatures were 1020 °C, 1040 °C and 1060 °C for 30 min, followed by quenching with oil. Then, the tempering temperatures were 570 °C, 590 °C and 610 °C for 120 min, followed by quenching with air cooling to obtain tempered martensite with embedded fine carbides.

To study the microstructure of the H13 electroslag steel, the sample was inlaid and polished until the surface was smooth and scratch-free. The surfaces of the H13 steels with different heat treatment processes were etched with a 4% nitric acid alcohol solution prior to imaging. The prior austenite grain (PAG) sizes were visualized by chemical thermal etching. The polished sample was immersed in 100 ml of saturated picric acid solution with 0.05 ml hydrochloric acid and 0.02 g sodium dodecyl sulfate at 60 °C in a thermostatic water bath for 60–70 s. Then, the PAG sizes were analyzed and counted with optical microscopy (OM, Leica DM2700) and Image-Pro Plus software, respectively. Scanning electron microscopy (SEM, Quanta 450) was used to observe the fracture surface of the Charpy V-notch impact specimens and tensile specimens.

Transmission electron microscopy (TEM, FEI Tecnai T12) was used to observe the fine structure of the H13 steels.

The carbide powder for x-ray diffraction (XRD) analysis was extracted by using a solution with 10 vol.% hydrochloric acid and 90 vol.% methanol, the current was maintained at 0.15–0.2 A, and the electrolysis time was approximately 12 h. The undissolved carbides in the H13 steel with different heat treatments were characterized using x-ray diffraction (XRD, Proto iXRD Combo) with Cu-K $\alpha$  radiation ( $\lambda = 1.5406 \text{ \AA}$ ), a scanning angle from 20° to 100° and a scanning speed of 1°/min.

The tensile specimens were prepared according to the national standard GB228.1-2010 that specifies the tensile specimen size. The size of the specimen is shown in Fig. 2. The test was carried out using a ZwickRoell Xte 051-JW tensile tester with a preload of 2 MPa and a load at strain rate with a loading speed of 0.00025/s.

The microhardness tests were carried out on an HX-1000TM semiautomatic microindentation hardness testing system according to national standard GB/T 4340.1-2009. The impact specimens were processed into standard Charpy V-notch specimens. The impact test was carried out on a JB-300B semiautomatic impact tester in accordance with national standard GB/T 229-2007. The lateral impact energy was measured because the lateral performance of H13 steel is very weak.

## 3. Results and Discussion

### 3.1 Effects of Quenching Temperature

**3.1.1 Microstructure Analysis.** Figure 3(a), (b) and (c) shows the microstructures of the H13 steel quenched at 1020, 1040 and 1060 °C, respectively. It can be observed that the microstructures of quenched samples comprise lath martensite. Moreover, as the quenching temperature increases from 1020 to

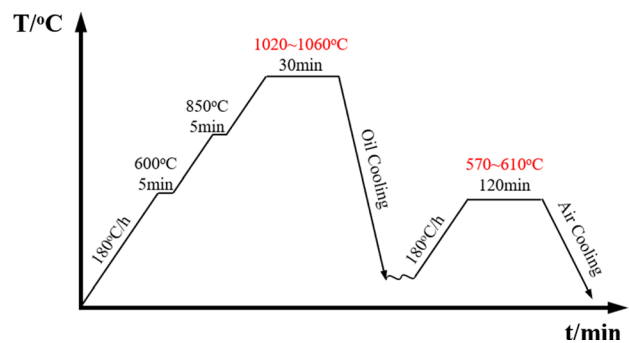


Fig. 1 Diagram of quenching and tempering heat treatment process

Table 1 Chemical composition of the H13 steel/wt.%

No.	C	Cr	Mo	V	Si	Mn	P	S
Test	0.39	5.09	1.45	0.92	1.07	0.34	0.011	0.0017
Standard	0.32–0.45	4.75–5.50	1.10–1.75	0.80–1.20	0.80–1.20	0.20–0.50	≤ 0.03	≤ 0.03

1060 °C, the martensite laths in the quenched state samples gradually decrease in width. Figure 3(d), (e) and (f) shows the microstructures of the H13 steel in the quenched and tempered states at the tempering temperatures of 1020, 1040 and 1060 °C, respectively. The microstructures of the tempered state samples comprise tempered martensite, and the martensite laths have recovered to some extent.

The average prior austenite grain sizes (PAGs) were counted to investigate the internal relationships among the grain sizes and mechanical properties, as shown in Fig. 4. Figure 4(a), (b) and (c) shows that the prior austenite grains coarsen as the quenching temperature increases. The statistical results show that the prior austenite grain sizes are 10.34, 10.48 and 12.21 μm with quenching temperatures of 1020, 1040 and 1060 °C, respectively. That is, as the quenching temperature increases, the prior austenite grain size increases and the grain

growth rate increases. The austenite grain growth rate is proportional to the heating temperature as follows (Ref 16):

$$V_D \propto D_0 \exp\left(-\frac{Q}{RT}\right) \quad (\text{Eq 1})$$

where  $V_D$  is the austenite grain growth rate,  $D_0$  is the diffusion constant,  $Q$  is the activation energy,  $R$  is the Boltzmann constant and  $T$  is the heating temperature.

As the quenching temperature  $T$  increases, the atomic diffusion activation energy  $Q$  decreases, and the growth rate  $V_D$  increases, so the prior austenite grains continue to coarsen as the quenching temperature increases, which is consistent with the statistical results, as shown in Fig. 4(d), (e) and (f). When the quenching temperature is 1020 °C, the PAGs are 10.34 μm, and with a quenching temperature of 1040 °C, the PAGs are 10.48 μm. The PAGs are essentially unchanged when the quenching temperature is no more than 1040 °C. When the quenching temperature exceeds 1060 °C, the prior austenite grains grow rapidly, and the PAGs are as large as 12.48 μm. When the quenching temperature exceeds a certain value, the second precipitated phase particles that inhibit the growth of the austenite grains begin to dissolve, and therefore, the pinning effects for the second precipitated phase particles are weakened, so the grain growth rates accelerate (Ref 17). Figure 4(d), (e) and (f) shows that the grain size distributions are basically in accordance with a Gauss normal distribution, and the proportion of large grains ( $\geq 15 \mu\text{m}$ ) increases remarkably when the quenching temperature is as high as 1060 °C. The volume fraction of large grains ( $\geq 15 \mu\text{m}$ ) is 18.69% with a quenching temperature of 1060 °C, and the volume fraction is 9.67% with a quenching temperature of 1020 °C.

**3.1.2 Mechanical Properties.** Figure 5 shows the relationships among the mechanical properties and quenching temperature for the H13 steel at different quenching temperatures. The yield strength and tensile strength increase with

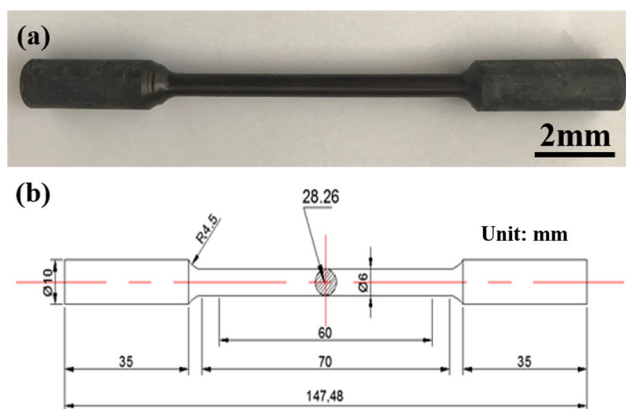


**Fig. 2** (a) Morphology of the tensile specimen and (b) dimensions of the tensile specimen

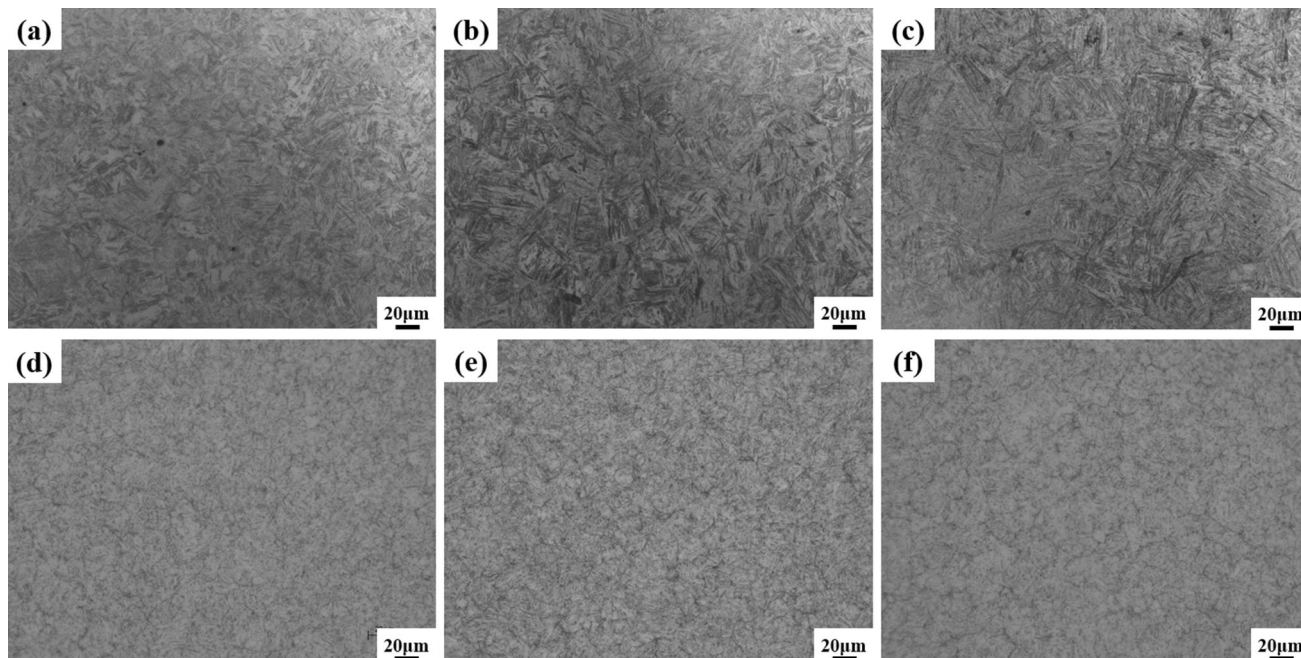


**Fig. 3** Microstructures of the H13 steels in (a), (b), (c) quenched and (d), (e), (f) quenched and tempered states at different quenching temperatures: (a), (d) 1020 °C; (b), (e) 1040 °C; and (c), (f) 1060 °C

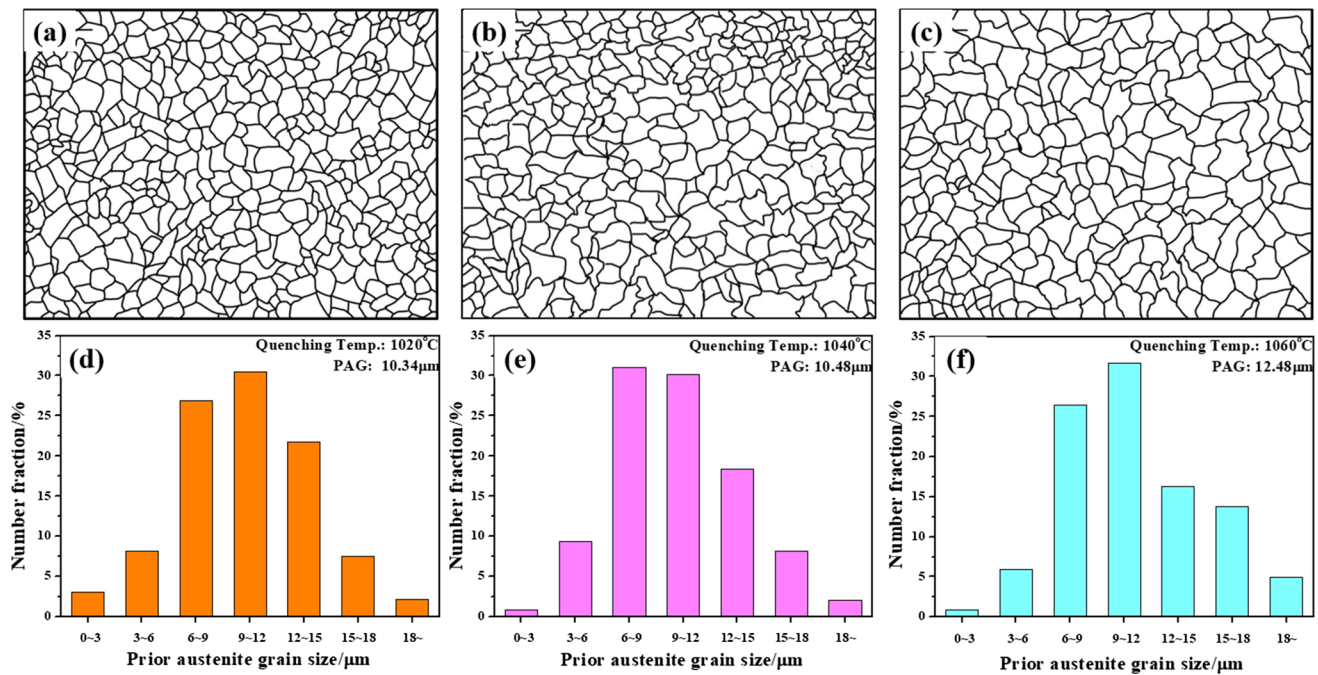


**Fig. 4** (a), (b), (c) Prior austenite grain patterns and (d), (e), (f) grain size distributions of the H13 steel in quenched and tempered states at different quenching temperatures of (a), (d) 1020 °C; (b), (e) 1040 °C; and (c), (f) 1060 °C

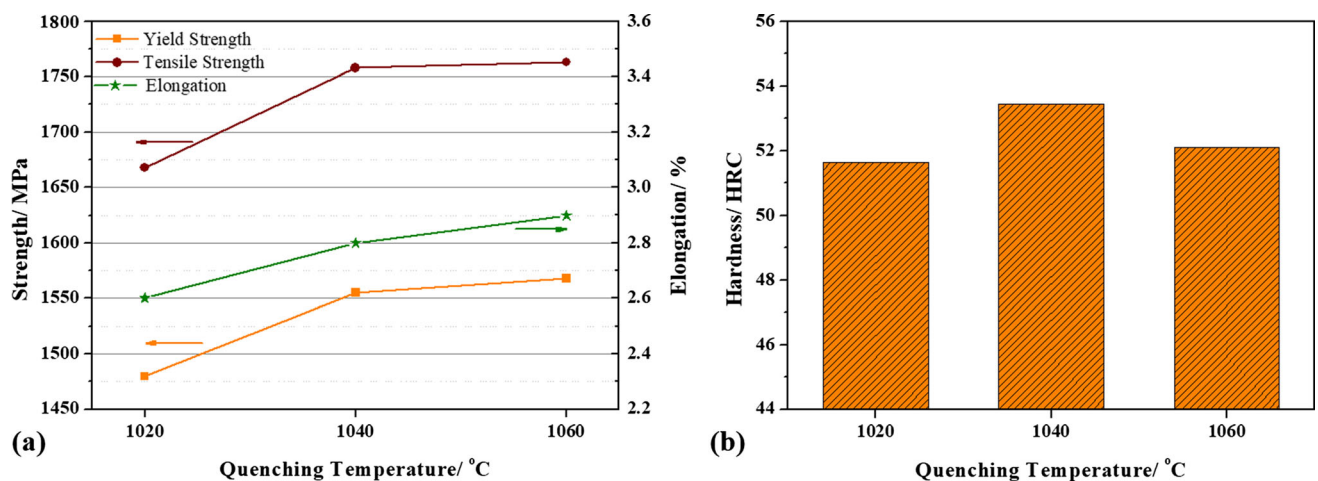


**Fig. 5** (a) Tensile properties and (b) hardness of H13 steels in quenched and tempered states at different quenching temperatures

increasing quenching temperature, as shown in Fig. 5(a). Additionally, the growth rate for the strength decreases with increasing temperature. When the quenching temperature is as high as 1060 °C, the yield strength and tensile strength of the H13 steel are the highest herein and are 1568 MPa and 1758 MPa, respectively. Correspondingly, the hardness of the H13 steel also tends to increase with increasing temperature. When the quenching temperature is 1040 °C, the hardness of the H13 steel is 53.45 HRC, and then, it decreases slightly, as shown in Fig. 5(b).

The elongation of the H13 steel increases with increasing quenching temperature and reaches a maximum of 2.9% with a quenching temperature of 1060 °C, as shown in Fig. 5(a). However, as the quenching temperature increases, the prior austenite grains continue to coarsen, resulting in a continuous decline in the impact energy, as listed in Table 2. The impact

**Table 2** Impact energy of the H13 steel in quenched and tempered states at different quenching temperatures

Quenching temp, °C	1020	1040	1060
$A_{KV}$ , J	28.0	22.0	14.3

energy reaches a maximum of 28 J at 1020 °C. When the quenching temperature is 1020 °C, the average austenite grain size is the smallest herein, and the proportion of small grains (3.04%) is significantly higher than the value of 0.91% at 1040 °C, which is the sample with the best impact toughness herein. When the quenching temperature rises to 1040 °C, the lateral impact energy decreases to 22 J, which is a reduction of 21.4%. When the quenching temperature rises to 1060 °C, the

original austenite grain size is obviously coarsened, the proportion of large grains ( $\sim 15$ ) increases from 10.16% at 1040 °C to 18.69%, and the impact energy is reduced by 48.9% to 14.3 J. It can be seen that as the quenching temperature increases, the plasticity of the H13 steel increases, while the toughness decreases, which substantially affects the performance.

Figure 6 shows the impact fracture morphologies of the H13 steels at different quenching temperatures. The macroscopic fracture morphologies are almost flat, with fibrous zones, radial zones and shear lips in them, as shown in Fig. 6(a), (b) and (c). Additionally, there are typical brittle fracture characteristics, and the area of the radiation zone is the largest herein when the quenching temperature is 1020 °C. Figure 6(d) shows an obvious step river-like pattern, with cleavage facets around them, as shown in Fig. 6(d) with the yellow arrow. As the quenching temperature increases, the number of ligaments on the impact fracture surfaces decreases gradually, which is consistent with the impact energy. When the quenching temperature increases to 1060 °C, there is a certain amount of voids on the fracture surfaces.

Figure 7 shows the tensile fracture morphologies of the H13 steels at different quenching temperatures. The tensile fracture sections are relatively flat with almost no necking. As the quenching temperature increases, the source of the crack moves from the edge toward the center slowly, with the fibrous zone area increasing gradually, as shown in Fig. 7(a), (b) and (c). Figure 7(d), (e) and (f) shows the fracture morphologies of the radial zone in detail. The cleavage facets decrease as the quenching temperature increases, as shown in Fig. 7 with the yellow arrows. When the quenching temperature is as high as 1060 °C, the fracture mode is microvoid coalescence fracture.

The mechanical properties of testing show that the yield strength increases with increasing quenching temperature. The strength of the material is mainly due to the combination of four basic strengthening mechanisms. According to the extended

Hall–Petch relationship (Ref 18), the relationship between yield strength and each strengthening mode is:

$$\sigma_y = \sigma_0 + \Delta\sigma_{ss} + \Delta\sigma_d + \Delta\sigma_p + K \cdot d^{-1/2} \quad (\text{Eq 2})$$

where  $\sigma_0$  is the lattice resistance,  $\Delta\sigma_{ss}$  is the solid solution strengthening increment,  $\Delta\sigma_d$  is the dislocation strengthening increment,  $\Delta\sigma_p$  is the precipitation strengthening increment and  $K \cdot d^{-1/2}$  is the fine-grain strengthening increment.  $K$  is a constant, and  $d$  is the average grain size. Since the tempering temperatures of the samples are the same, the solid solution strengthening effects ( $\Delta\sigma_{ss}$ ) are basically the same. Figure 3 shows that the size and distribution of the carbides are basically the same at different quenching temperatures, and the quenching temperature has no obvious effect on the dislocations. Moreover, the tempering treatment remarkably reduces the dislocation density (Ref 19, 20), so the effects of dislocation strengthening ( $\Delta\sigma_d$ ) and precipitation strengthening ( $\Delta\sigma_p$ ) are also small. In summary, fine-grain strengthening ( $K \cdot d^{-1/2}$ ) affects the strength ( $\Delta\sigma_y$ ) more so than the other mechanisms. However, the average grain size is negatively correlated with the strength and does not satisfy the Hall–Petch relationship, as shown in Fig. 4(d), (e) and (f). The Hall–Petch formula describes the relationship between the average grain size ( $d$ ) and strength ( $\Delta\sigma_y$ ). The prior austenite grains can be divided into several martensite packets with the same habits, but different orientations. The packet can be further divided into several blocks with similar orientations. The subgrain structure in a block is called a lath, where the packet and block belong to a high-angle grain boundary, and the lath belongs to a low-angle grain boundary (Ref 21). Marder and Marder (Ref 22) proposed a martensite lath, packet and block model. In this model, martensite has multiple structures, but the controlling factor for its strength is currently inconclusive (Ref 23). According to the literature (Ref 24), low-angle grain boundaries can be an effective obstacle for dislocation motion, leading to strengthening and a reduction in the number stress concentra-

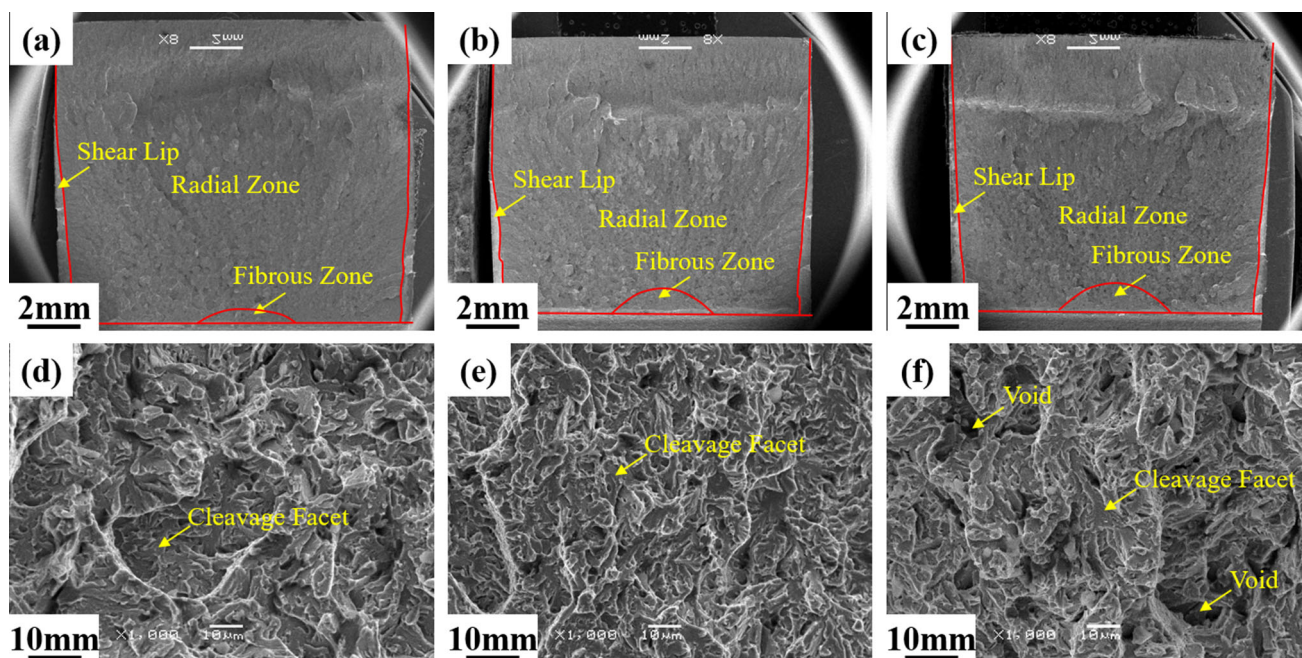


**Fig. 6** Impact fracture morphologies of the H13 steels in quenched and tempered states at different quenching temperatures: (a) 1020 °C, 8 $\times$ ; (b) 1040 °C, 8 $\times$ ; (c) 1060 °C, 8 $\times$ ; (d) 1020 °C, 1000 $\times$ ; (e) 1040 °C, 1000 $\times$ ; and (f) 1060 °C, 1000 $\times$

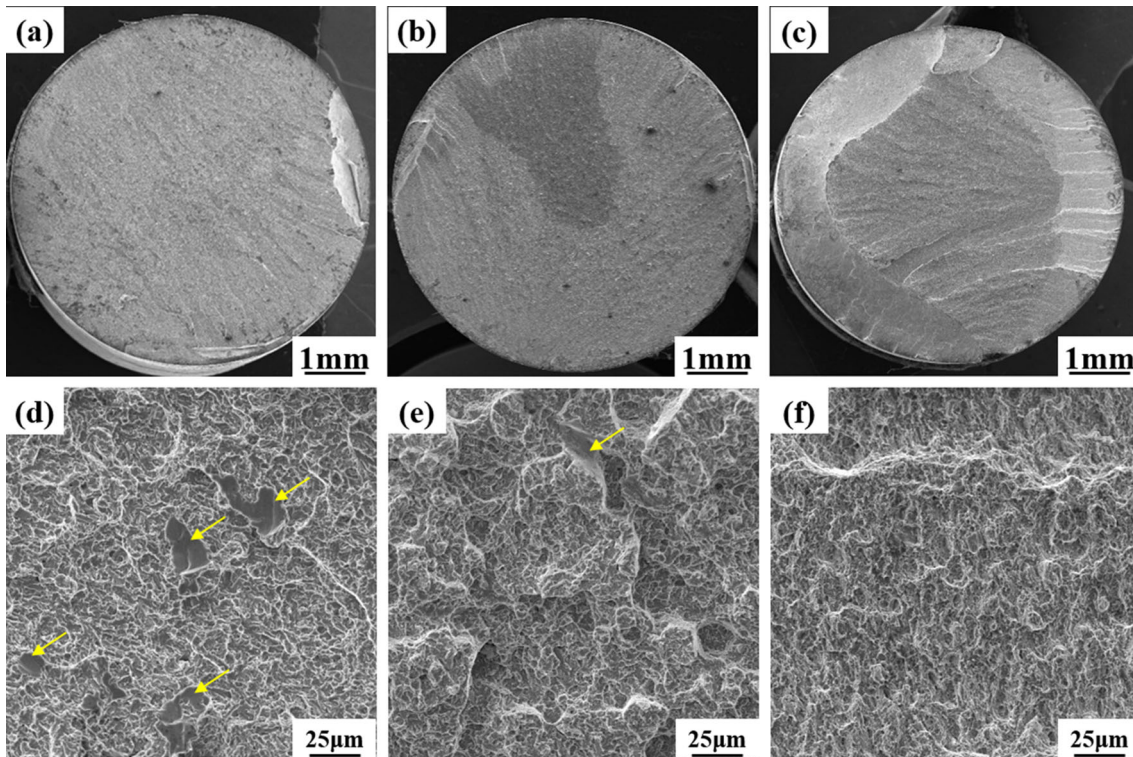


**Fig. 7** Tensile fracture morphologies of the H13 steels in quenched and tempered states at different quenching temperatures: (a) 1020 °C, 8×; (b) 1040 °C, 8×; (c) 1060 °C, 8×; (d) 1020 °C, 1000×; (e) 1040 °C, 1000×; and (f) 1060 °C, 1000×

**Table 3** Lath widths in the H13 steel at different quenching temperatures

Quenching temp, °C	1020	1040	1060
Lath width, nm	310	290	260

tions. Low-angle grain boundaries show an improved ability to adjust the strength and ductility.

Therefore, a statistical study on the widths of the low-angle grain boundary laths was conducted by TEM. The results are listed in Table 3, and the martensite lath morphologies are shown in Fig. 8. The lath width gradually decreases with increasing quenching temperature, the dislocation nets are distributed around the lath martensite, and the density is high. Therefore, in this test, the lath width and strength satisfy the Hall–Petch relationship, and the lath width is considered to control the strength of H13 steel.

Figure 9 shows the dependence of the yield strength and tensile strength on the prior austenite grain size and lath size in the H13 steel. The lath width increases linearly, and the prior austenite grain size decreases linearly with the strength at different quenching temperatures. The lath width and strength are positively correlated, which is in accordance with the Hall–Petch relationship; therefore, the lath width controls the strength of H13 steel.

### 3.2 Effect of the Tempering Temperature

**3.2.1 Microstructure Analysis.** Figure 10 shows the microstructures of the H13 steel after quenching and tempering with different tempering temperatures of 570, 590 and 610 °C.

The microstructures after quenching and tempering treatment comprise mainly martensite. As the tempering temperature increases, the martensite laths gradually recover.

Figure 10(d) shows that the carbides precipitate preferentially along the martensite lath boundaries after being tempered at 570 °C. The carbides precipitate preferentially along the interface because of low thermal activation energy. Moreover, the carbides are mainly strip-like with high aspect ratios, as marked with yellow arrows. The strip-like carbides are approximately 400 nm in length and 50 nm in width, as shown in Fig. 10(g). Moreover, as the tempering temperature increases, the carbides gradually change from a slender strip to a round granular shape, as shown in Fig. 10(d), (e) and (f). The slender strip-like carbides are marked with yellow arrows, and the round granular carbides are marked with red arrows. The round granular carbides are approximately 100–150 nm in diameter, as shown in Fig. 10(h) and (i) with the red arrows. The number of the slender strip-like carbides decreases, while the number of the round granular carbides increases with increasing tempering temperature. Finally, when the tempering temperature reaches 610 °C, the carbides disperse in the matrix. This type of structure reduces the strength and hardness, but improves the toughness of the steel.

Since the hardness of the H13 steels with different tempering treatments is closely related to the number of the carbides, carbide extraction tests are applied to analyze the phase structure of the carbides, as shown in Fig. 11.

Figure 11 shows that the carbides in the quenched and tempered H13 steel are mainly Cr-rich carbides, including  $M_{23}C_6$  ( $Cr_{23}C_6$ ),  $M_7C_3$  ( $Cr_7C_3$ ) and MC (VC). According to the results, the number of VC particles decreases with increasing tempering temperature, while the number of  $Cr_{23}C_6$  particles

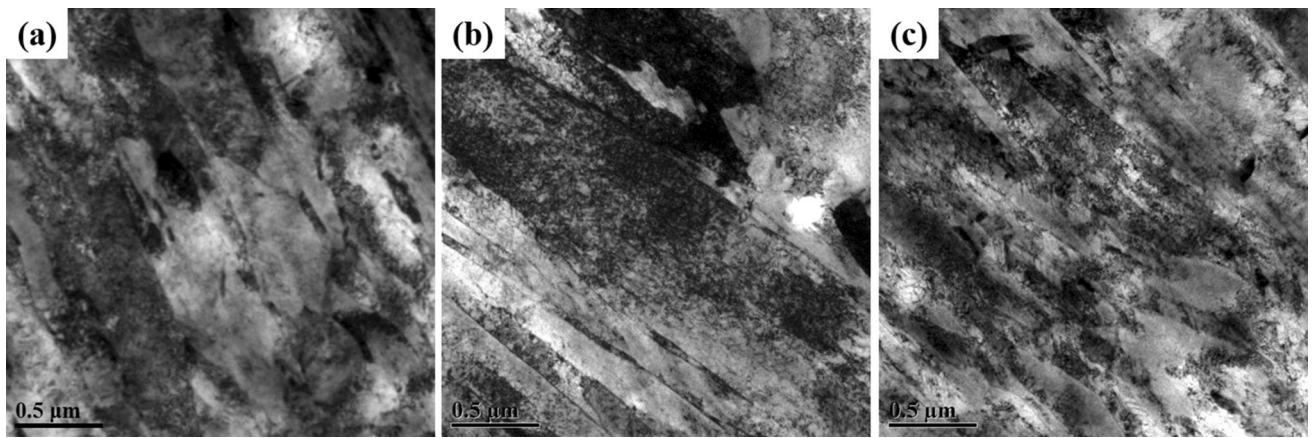


**Fig. 8** Transmission electron microscopy of H13 steel in quenched and tempered states at different quenching temperatures: (a) 1020 °C, (b) 1040 °C and (c) 1060 °C

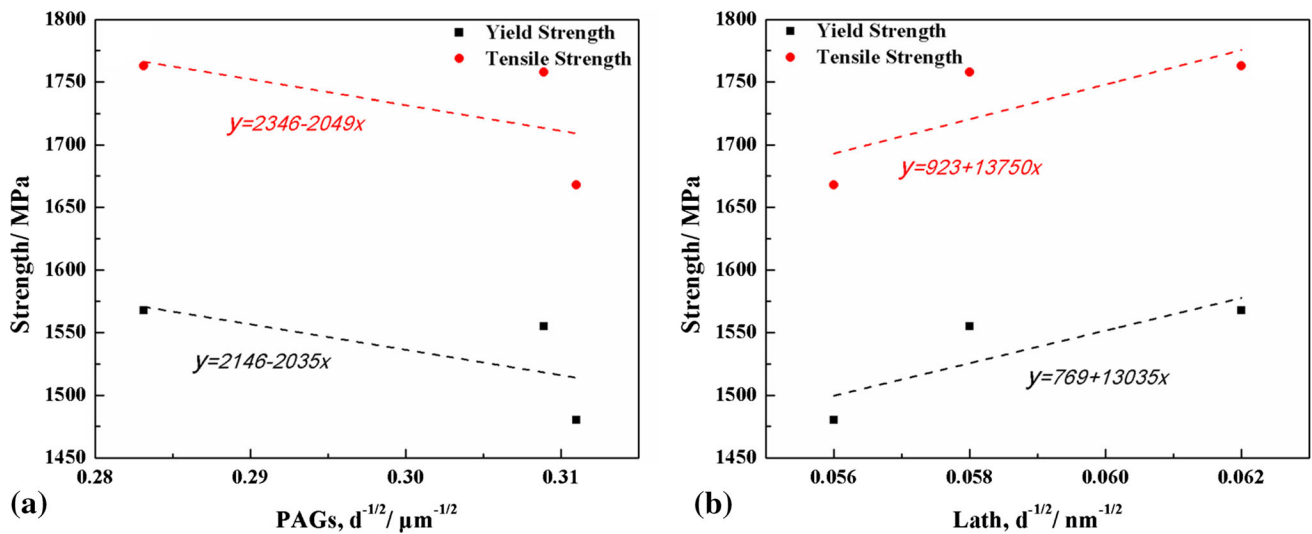


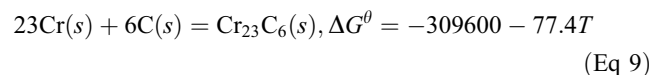
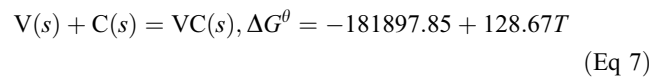
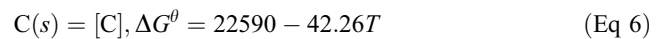
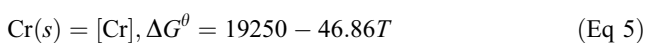
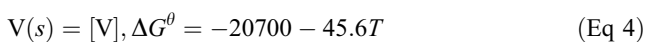
**Fig. 9** Dependence of the yield strength and tensile strength on the (a) prior austenite grain size and (b) lath size in the H13 steel

increases. The  $\text{Cr}_7\text{C}_3$  phase dissolves when the tempering temperature is above 590 °C.

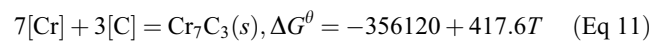
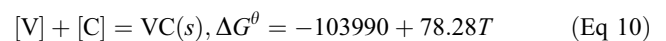
The thermodynamic calculation of the main carbides is based on the principle of metallurgical thermodynamics. During the cooling process of molten steel, the solubility of carbides is continuously reduced. When the actual solubility product of the precipitated elements is larger than the equilibrium solubility product, the carbides precipitate out of the liquid phase directly. The metallic element M in the molten steel reacts with the nonmetallic element N to form a precipitation reaction formula of  $\text{M}_x\text{N}_y$ :



According to the literature (Ref 25, 26), the thermodynamic data for vanadium, chromium and carbon are as follows:



From formulas 4 to 9, an equilibrium reaction formula and a standard Gibbs free energy function for carbides and dissolved elements in the liquid phase H13 steel are obtained, as shown in Eq 10 to 12:



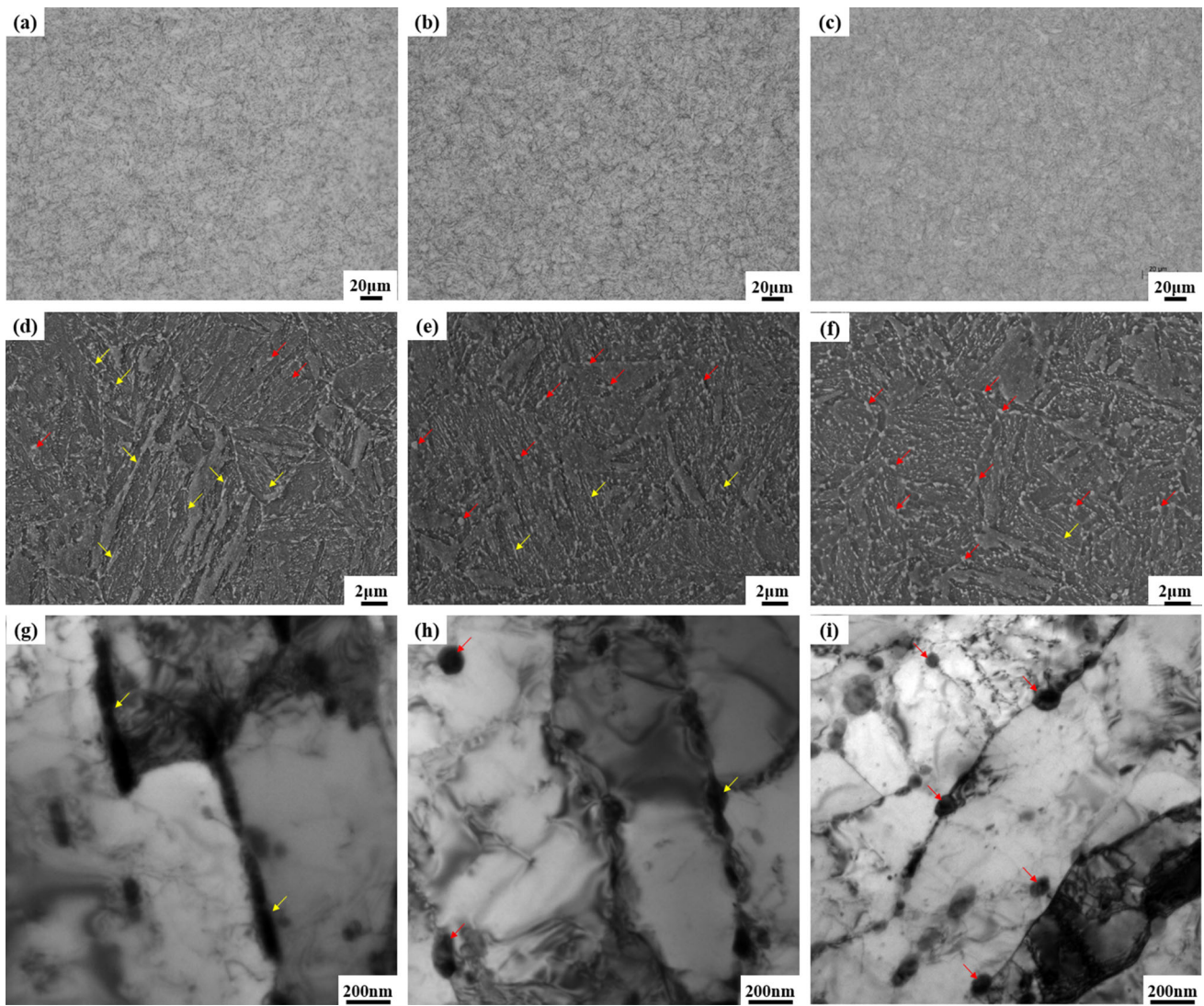
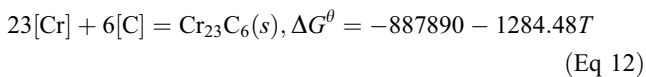


**Fig. 10** Microstructures of the H13 steels in quenched and tempered states at different tempering temperatures: (a), (d), (g) 570 °C; (b), (e), (h) 590 °C; and (c), (f), (i) 610 °C



The equilibrium solubility products, in which carbides precipitate at a temperature above the liquidus, are obtained, as shown in Eq 13 to 15:

$$\ln(\omega[\text{V}] \cdot \omega[\text{C}]) = 10.21 - \frac{12508}{T} \quad (\text{Eq } 13)$$

$$\ln(\omega[\text{Cr}]^7 \cdot \omega[\text{C}]^3) = 54.43 - \frac{42834}{T} \quad (\text{Eq } 14)$$

$$\ln(\omega[\text{Cr}]^{23} \cdot \omega[\text{C}]^6) = 158.08 - \frac{106794.56}{T} \quad (\text{Eq } 15)$$

The chemical compositions are listed in Table 1. The results show that the precipitation temperature for VC is 1112.37 K, the precipitation temperature for  $\text{Cr}_7\text{C}_3$  is 933.25 K, and the precipitation temperature for  $\text{Cr}_{23}\text{C}_6$  is 845.07 K. That is, the

VC phases precipitate first, while the precipitation temperatures for  $\text{Cr}_7\text{C}_3$  and  $\text{Cr}_{23}\text{C}_6$  are similar.

Relevant literature reports indicate that MC and  $\text{M}_{23}\text{C}_6$  phases are spherical, the size of the MC phase is small, while the  $\text{M}_{23}\text{C}_6$  phase is large (Ref 27, 28). The shape of the  $\text{M}_7\text{C}_3$  phase exhibits a polygonized structure, and the  $\text{M}_7\text{C}_3$  phase is unstable and is converted into the  $\text{M}_{23}\text{C}_6$  phase at a certain temperature; then, the  $\text{M}_{23}\text{C}_6$  phase is easy coarsened (Ref 29). Upon considering the microstructure and XRD results, it is clear that the round granular carbides are mainly the VC and  $\text{Cr}_{23}\text{C}_6$  phases, while the block-like carbides are mainly the  $\text{Cr}_7\text{C}_3$  phase. With increasing tempering temperature, the  $\text{Cr}_7\text{C}_3$  phase gradually decreases and disappears, while the  $\text{Cr}_{23}\text{C}_6$  phase increases correspondingly. As shown in Fig. 10, the red arrow indicates a round granular carbide, and the yellow arrow indicates a slender strip-like carbide. It is obvious that as the tempering temperature increases, the long strip-like carbides decompose into round granular carbides gradually and then tend to coarsen. The mechanisms for the disconnection include dissolution-induced breaking, capillary-induced breaking and



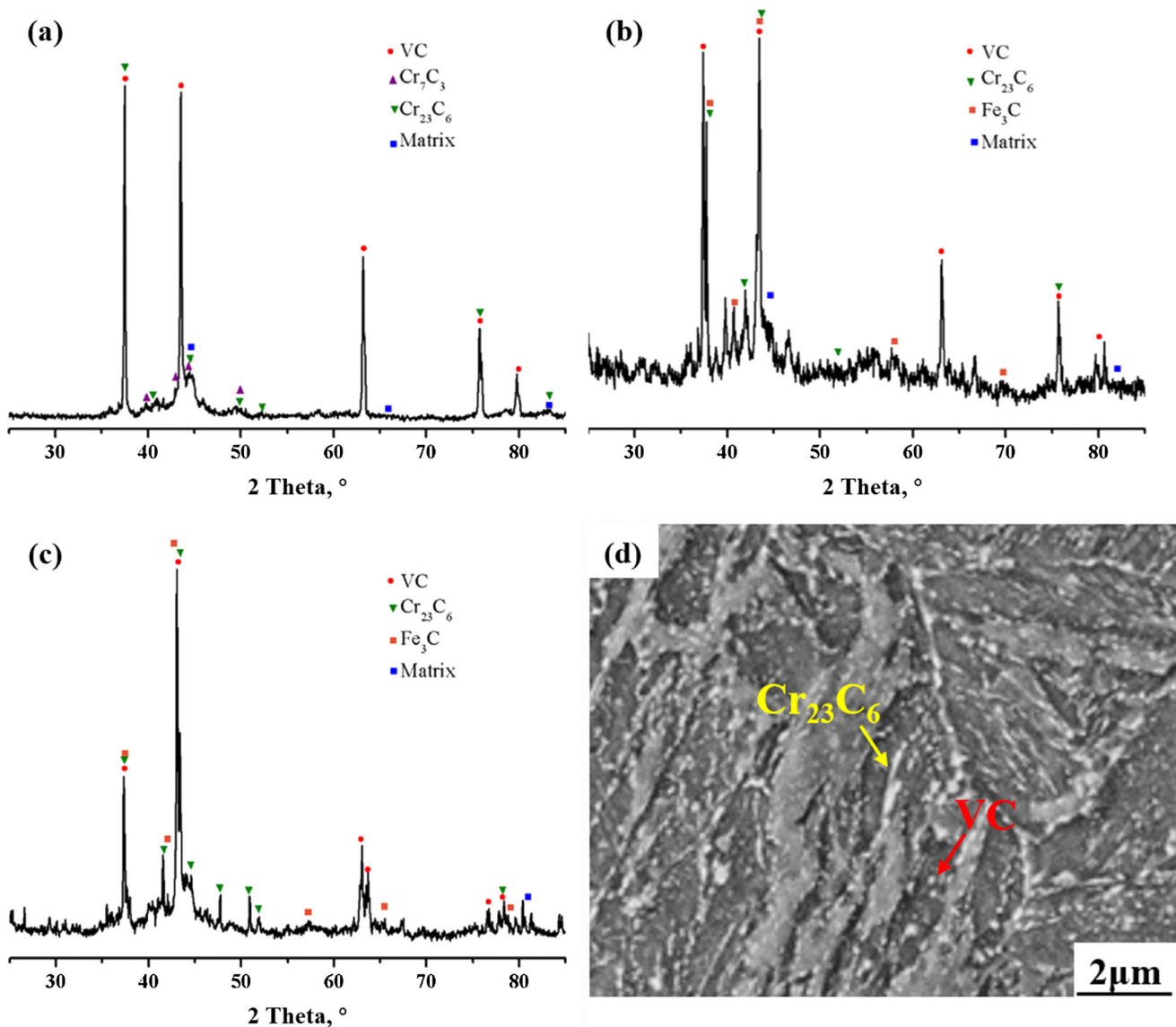


**Fig. 11** XRD analysis of the carbides in the H13 steel in quenched and tempered states with different tempering temperatures: (a) 570 °C, (b) 590 °C and (c) 610 °C and (d) SEM image of the carbides

comprehensive control breaking (Ref 30). The element concentrations in the different types of carbides are different; then, the carbides dissolve or break preferentially from their locations or defects, and finally, the rodlike carbides spheroidize gradually (Ref 31). It can also be seen from the figure that the edges of the long carbides are saw-toothed, the depth of the zigzag patterns increases and they decompose into a circular Cr<sub>23</sub>C<sub>6</sub> particles. The Cr<sub>23</sub>C<sub>6</sub> phase coarsens readily, resulting in a decrease in the hardness and strength of the H13 steel.

**3.2.2 Mechanical Properties.** Figure 12 shows the relationship between the mechanical properties of the H13 steels after quenching and tempering at different tempering temperatures. Figure 12(a) shows that the elongation increases with increasing tempering temperature, and the elongation increases significantly from 2.1 to 5.9%. As the tempering temperature increases, the strength and hardness of the H13 steels decrease

continuously. The hardness at the 610 °C tempering temperature is approximately 6% lower than that at the 590 °C tempering temperature. This is because as the tempering temperature continues to increase, the Cr<sub>23</sub>C<sub>6</sub> content continues to increase, and the easily coarsened Cr<sub>23</sub>C<sub>6</sub> carbides reduce the hardness of the H13 steel.

The impact toughness increases with increasing tempering temperature owing to a decrease in the dislocation density. The impact toughness for H13 tempered at 610 °C is the best herein, while the hardness is obviously insufficient, as listed in Table 4 and Fig. 12(b). Figure 13 shows the impact fracture morphologies of the H13 steels at different tempering temperatures. When the sample is tempered at 570 °C (Fig. 13a), the radial zone is the largest herein, while the fibrous zone is the smallest, and the impact fracture morphology indicates brittle fracture. With an increase in the tempering temperature, the area of the shear lip increases gradually, while the area of the

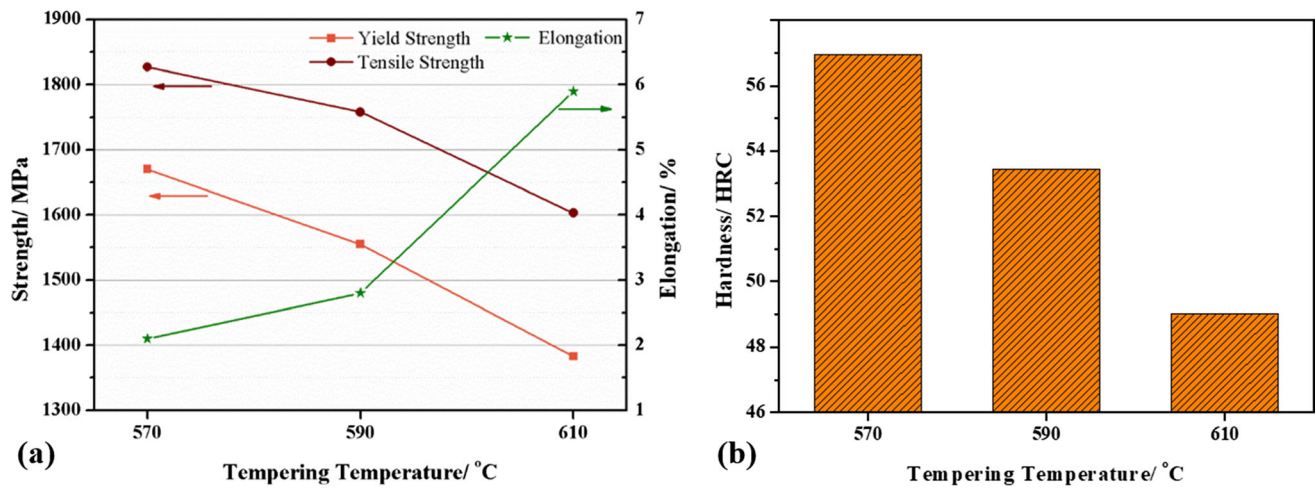


Fig. 12 (a) Tensile properties and (b) hardness of the H13 steels in quenched and tempered states at different tempering temperatures

Table 4 Impact energy of the H13 steel in quenched and tempered states at different tempering temperatures

Tempering temp, °C	570	590	610
$A_{KV}$ , J	17.0	22.0	28.0

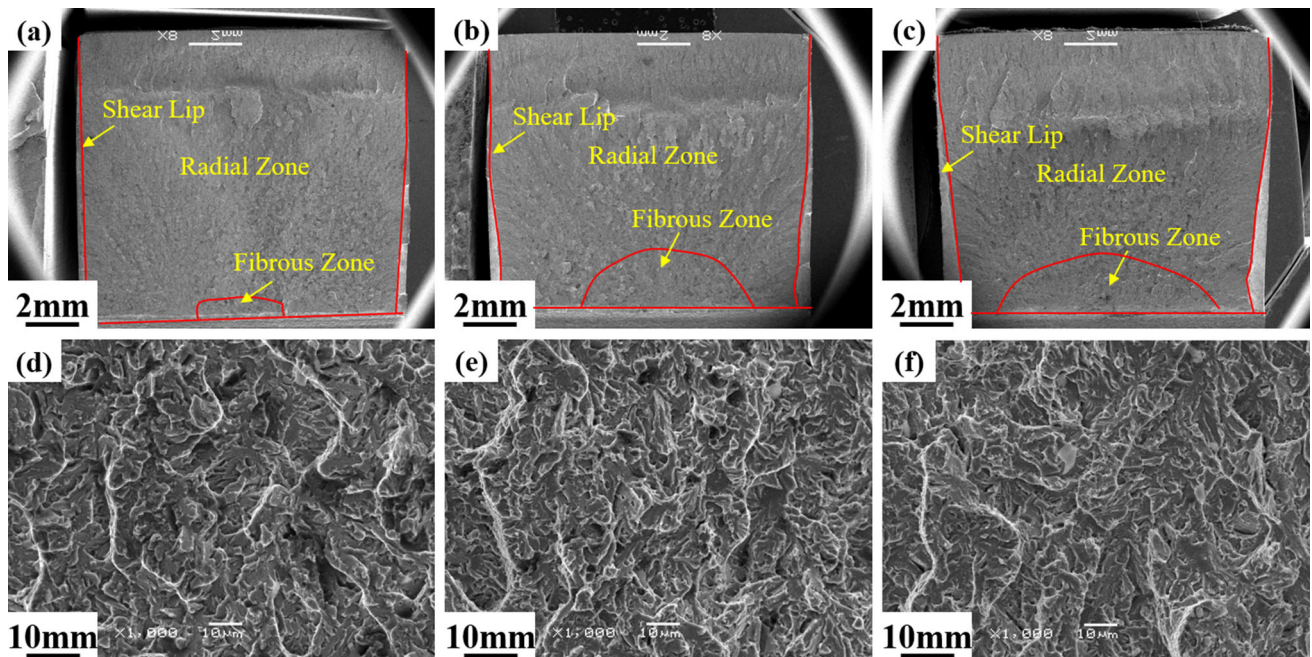


Fig. 13 Impact fracture morphologies of the H13 steels in quenched and tempered states at different tempering temperatures: (a) 570 °C, 8×; (b) 590 °C, 8×; (c) 610 °C, 8×; (d) 570 °C, 2500×; (e) 590 °C, 2500×; and (f) 610 °C, 2500×

radial zone decreases accordingly, indicating that the fracture mode gradually evolves from brittle fracture to ductile fracture. Figure 13(d), (e) and (f) shows that the fracture surfaces exhibit quasi-cleavage fractures, and the dimple size for the H13 steel tempered at 610 °C is larger than that at 570 °C. An increased dimple size means that the sample demonstrated an improved plastic deformation; that is, the impact toughness increased (Ref 19).

The increase in the toughness of the H13 steel is related to the evolution of the carbides. When the tempering temperature increases from 570 to 610 °C, the morphology of the carbides changes from a long strip to a short rod and finally to a globular shape. At the same time, the distribution of the carbides gradually changes from a continuous distribution along the martensite laths to a dispersed distribution. As the tempering temperature increases, the carbides decrease in length, and the

stress concentration decreases significantly, resulting in a significant increase in the crack formation energy. Moreover, since the carbides are no longer continuous, crack propagation becomes difficult, and thus, the crack propagation energy also increases.

## 4. Conclusion

In this paper, the optimized heat treatment process for H13 steel for high-temperature disk springs is studied. Analyses using single variables are applied to investigate the effect of the quenching and tempering temperatures on the microstructures and mechanical properties of the H13 steel. The main conclusions are as follows:

1. As the quenching temperature increases, the prior austenite grain sizes increase, the lath width decreases, and the yield strength increases. The lath width controls the strength of the H13 steel, which is in accordance with the Hall–Petch relationship.
2. With increasing tempering temperature, the block-like  $\text{Cr}_7\text{C}_3$  phase is converted to a round granular  $\text{Cr}_{23}\text{C}_6$  phase, and then, the  $\text{Cr}_{23}\text{C}_6$  phase tends to coarsen, resulting in a decreased hardness with a high impact toughness and elongation.
3. When the quenching temperature is 1040 °C and the tempering temperature is 570 °C, the H13 steel after quenching and tempering has a uniform microstructure with good strength and toughness.

## Acknowledgments

This work was supported by the National Natural Science Foundation of China (No. 11772147), the Natural Science Foundation of the Jiangsu Higher Education Institutions of China (Grant No. 18KJB460016) and the Introduce Talent Special Funding for Scientific Research at Nanjing Tech University (Grant No. 39802124).

## References

1. L.A. Dobrzanski, J. Mazurkiewicz, E. Hajduczek, and J. Madejski, Comparison of the Thermal Fatigue Resistance and Structure of the 47CrMoWVTiCeZr16-26-8 Hot-Work Tool Steel with X40CrMoV5-1 Type One, *J. Mater. Process. Technol.*, 2001, **113**(1–3), p 527–538
2. A. Persson, S. Hogmark, and J. Bergstrom, Simulation and Evaluation of Thermal Fatigue Cracking of Hot Work Tool Steels, *Int. J. Fatigue*, 2004, **26**(10), p 1095–1107
3. A. Persson, S. Hogmark, and J. Bergstrom, Failure Modes in Field-Tested Brass Die Casting Dies, *J. Mater. Process. Technol.*, 2004, **148**(1), p 108–118
4. Y.F. Wang, Z.C. Liu, and W.B. Fan, The Band Structure of H13 Steel and Its Elimination Method, *Shanghai Met.*, 2005, **06**, p 43–45
5. H. Jimenez, D.M. Devia, V. Benavides, A. Devia, Y.C. Arango, and P.J. Arando, Thermal Protection of H13 Steel by Growth of (TiAl)N Films by PAPVD Pulsed arc Technique, *Mater. Charact.*, 2008, **59**, p 1070–1077
6. Q. Tong, X.C. Wu, and N. Min, Research on Hot-Working Die Steel SDH3 with High Hot Strength, *J. Iron Steel*, 2010, **22**, p 50–54
7. S. Li, X.C. Wu, X.X. Li, J.W. Li, and X.J. He, Wear Characteristics of Mo-W-Type Hot-Work Steel at High Temperature, *Tribol. Lett.*, 2016, **64**(32), p 1–12
8. S. Li, X.C. Wu, S.H. Chen, and J.W. Li, Wear Resistance of H13 and a New Hot-Work Die Steel at High Temperature, *J. Mater. Eng. Perform.*, 2016, **25**, p 2993–3006
9. X.H. Pan and Z.C. Zhou, The Study of the Chemical Composition and Improvement and Development for the H13 Hot Work Die & Mold Steel, *Mold Manuf.*, 2006, **4**, p 78–85
10. P.S. Babu, Effects of Cryogenic Treatment on H13 Tool Steel—An Experimental Investigation, *Int. J. Metall. Mater.*, 2013, **3**, p 53–58
11. C. Xie, X. Wu, N. Min, and Y. Shen, Carbon Segregation Behavior of High Carbon High-Alloy Steel During Deep Cryogenic Treatment Using 3DAP, *Acta Metall. Sin.*, 2015, **15**, p 325–332
12. M. Pérez and F.J. Belzunce, The Effect of Deep Cryogenic Treatments on the Mechanical Properties of an AISI, H13 Steel, *Mater. Sci. Eng. A*, 2015, **624**, p 32–40
13. G.H. Yan, X.M. Huang, Y.Q. Wang et al., Effects of Heat Treatment on Mechanical Properties of H13 Steel, *Met. Sci. Heat Treat.*, 2010, **52**, p 393–395
14. J. Li, J. Li, L.L. Wang, and L.F. Li, Study on Carbide in Forged and Annealed H13 Hot Work Die Steel, *High Temp. Mater. Proc.*, 2015, **34**, p 593–598
15. L.A. Norstrom and N. Ohrberg, Development of Hot-Work Tool Steel for High-Temperature Applications, *Met. Technol.*, 1981, **8**, p 22–26
16. S.J. Fu, Influence of Quenching Temperature on Microstructure and Properties of 25MnV Steel, *Therm. Process.*, 2010, **39**(20), p 156–157
17. Y.R. Liu, D. Ye, Q.L. Yong, J. Su, K.Y. Zhao, and W. Jiang, Effect of Heat Treatment on Microstructure and Property of Cr13 Super Martensitic Stainless Steel, *J. Iron Steel Res. Int.*, 2011, **18**(11), p 60–66
18. D.W. Smith and R.F. Hehemann, Influence of Structural Parameters on the Yield Strength of Tempered Martensite and Lower Bainite, *J. Iron Steel Inst.*, 1971, **209**(5), p 478–481
19. H.H. Liu, P.X. Fu, H.W. Liu, C. Sun, X.P. Ma, and D.Z. Li, Microstructure Evolution and Mechanical Properties in 718H Pre-hardened Mold Steel During Tempering, *Mater. Sci. Eng. A*, 2018, **709**, p 181–192
20. P. Yan, Z. Liu, H. Bao, Y.Q. Weng, and W. Liu, Effect of Tempering Temperature on the Toughness of 9Cr-3W-3Co Martensitic Heat Resistant Steel, *Mater. Des.*, 2014, **54**, p 874–879
21. T. Maki, K. Tsuzaki, and I. Tamura, The Morphology of Microstructure Composed of Lath Martensites in steels, *Trans ISIJ*, 1980, **20**(4), p 207–214
22. J.M. Marder and A.R. Marder, The Morphology of Iron–Nickel Massive Martensite, *Trans. Am. Soc. Met.*, 1969, **62**(1), p 1–10
23. C.F. Wang, *Study on Strength and Toughness Structure Control Unit of Low Alloy Martensitic Steel*, Central Iron & Steel Research Institute, Beijing, 2008
24. S.J. Chen and Q. Yu, The Role of Angle Boundary in Deformation of Titanium and Its Size Effect, *Scr. Mater.*, 2019, **163**, p 148–151
25. Q.L. Yong, *The Second Phase of the Steel Materials*, Metallurgical Industry Press, Beijing, 2006
26. D.L. Ye and J.H. Hu, *Practical Inorganic Thermodynamic Data Manual*, 2nd ed., Metallurgical Industry Press, Beijing, 2002
27. N. Mebarki, D. Delagnes, P. Lamesle et al., Relationship Between Microstructure and Mechanical Properties of a 5% Cr Tempered Martensitic Tool Steel, *Mater. Sci. Eng., A*, 2004, **387–389**, p 171–175
28. D. Delagnes, P. Lamesle, M.H. Mathon et al., Influence of Silicon Content on the Precipitation of Secondary Carbides and Fatigue Properties of a 5% Cr Tempered Martensitic Steel, *Mater. Sci. Eng., A*, 2005, **394**, p 435–444
29. X.B. Hu, L. Li, X.C. Wu, and M. Zhang, Coarsening Behavior of M23C6 Carbides After Ageing or Thermal Fatigue in AISI, H13 Steel With Niobium, *Int. J. Fatigue*, 2006, **28**, p 175–182
30. Q. Ma, B.C. Liu, and Z.C. Wang, Breakup of Eutectic Carbide Network of White Cast Irons at High Temperatures, *J. Mater. Sci.*, 1995, **311**, p 3383–3386
31. W.Y. Zhang, Ostwald Growth of Spheroidal Carbide During Isothermal Spheroidization, *Mater. Sci. Technol.*, 1993, **1**(4), p 44–48

**Publisher's Note** Springer Nature remains neutral with regard to jurisdictional claims in published maps and institutional affiliations.